e-Bike Motor Design based on Analytical and Finite Element Performance Mapping

Chiara Contò and Nicola Bianchi

***Abstract*—This paper deals with a design procedure of an electric motor for e-bike. The motor topology is the typical permanent magnet synchronous machine. The study combines a preliminary analytical model and finite element analysis simulation to test different motor geometries. Experimental measures for different supplying conditions are presented. The performance is evaluated both through analytical models and finite element simulations. Some parameters are considered as variables analysing the geometries generated by their combinations. Torque, speed, power, losses and efficiency are mapped in order to map the capabilities in the whole parameter space.**

***Index Terms*—Electric bicycle, Electric motor design, Permanent magnet motors, Interior permanent magnet motors**

I. Introduction

Electric bicycles, or e-bikes [1], have gained popularity due to their environmental benefits and convenience. The e-bike market is projected to grow annually by 10 %, reaching nearly USD 48.5 billion by 2028 [2]. For Light Electric Vehicle (EV) mobility, high-performance electrical motors with high torque at low speeds and consistent output over a wide range are vital. Permanent Magnet Synchronous Motors (PMSMs) are the preferred choice for traction motors [3]. Brushless DC electric motors have received significant attention in the literature, with studies focusing on aspects such as modelling, comparisons, controller design, and motor analysis [4]–[8].

While Permanent Magnet (PM) motors stand as the optimal choice for traction applications, the escalated cost and diminishing availability of magnetic materials, particularly rare-earth PMs, stimulate the exploration of alternative solutions. Studies investigating the design of innovative motors tailored for e-bike applications can be found in the literature. For instance, [9] introduces a pioneering design for an in-hub outer rotor PM-assisted synchronous reluctance motor. This innovative design bolsters the capabilities of the synchronous reluctance machine by incorporating PMs into the rotor barriers. As a result, torque density experiences a notable 28 % enhancement, accompanied by simultaneous reductions in cogging torque (50 %) and torque ripple (8 %). Notably, this design contributes to a 40 % reduction in PM usage and associated costs when compared to a commercial brushless DC motor.

Authors are with University of Padova, Department of Industrial Engineering, Padova, Italy.

This study is partially supported by Department of Industrial Engineering, University of Padova, by means of the project SID BIRD224007 and partially carried out within the NEST - Network 4 Energy Sustainable Transition (D.D. 1243 02/08/2022, PE00000021) and the project is funded Project funded under the National Recovery and Resilience Plan (NRRP), Mission 4 Component 2 Investment 1.3 - Call for tender No. 1561 of 11.10.2022 of Ministero dell'Università e della Ricerca (MUR), funded by the European Union - NextGenerationEU.

This work focuses on the PM synchronous motor topology, which overcomes some limitations of reluctance machines and is increasingly popular in light EV applications. PM machines exhibit high torque density, particularly at low speeds, which is a current trend in the development of high-performance motors for e-bikes. In addition, considering e-bike application, fractional-slot non-overlapped coil windings [10], [11], which have a non-integral number of slots per pole per phase, are commonly employed. These windings have several advantages, such as being suitable for high-pole machines [12] and having reduced end-winding lengths, which leads to lower copper weight and Joule losses. However, they can cause a low winding factor or sub-harmonics in the magneto motive force which leads to additional rotor losses and torque ripple.

Literature mainly presents brushless dc electric motors [4]–[8]. An investigation into innovative electric motors for e-bikes can be found in [9]. This work introduces an in-hub outer rotor PM-assisted synchronous reluctance motor. Designed to enhance power density and reduce torque ripple, it achieves a 28% increase in torque density and reduces cogging torque and ripple by 50% and 8% respectively. Compared to commercial brushless DC motors, it reduces permanent magnet usage and costs by 40%, although with a slight decrease in efficiency.

Switched reluctance technology has gained attention as an alternative solution for e-bike propulsion systems. In [13] the feasibility of employing external rotor structures in in-wheel e-bike motors is investigated. By this way, the motor integration within the wheel hub is facilitated. Furthermore, [14] presents an optimized design approach for switched reluctance motors. The focus is achieving performance metrics and dimensional specifications similar to those observed in commercial permanent magnet e-bike motors.

Motors for e-bike applications require high performance and small size to facilitate assembly and reduce the final bulk of the bicycle. Additive manufacturing is gaining interest in these aspects because of its ability to easily fabricate components with complex geometries, high performance and reduced volumes. Some examples of small size printed motor prototypes can be found in [15], [16].

In literature few studies on PM synchronous motors for e-bike application can be found. In [17] a low cost ferrite based PM motor is presented, together with a planetary gear unit, which provides better overload capability. Some works concern axial flux synchronous motors, such as [18]–[20]. A few studies focus on PM machines employing high flux-density magnets [21], [22], that is actually the most common motor topology in the electric bicycle market. This can be observed in the Bosch official site [23], where the electric motor is shown, and the PM configuration can be spotted.

The primary objective of this study is to give a guideline for the electric motor design based on the preliminary results given in [24] and [25]. The PM synchronous machine is considered for such application.

This study introduces an approach to define the design limits of a Permanent Magnet Synchronous Motor (PMSM) specifically create for e-bike. An area where performance is enhanced is identified and the parameters responsible for this improvement are analysed. A specific motor geometry can be analysed both through analytical performance characteristics and Finite Element (FE) simulation. After confirming the accuracy of the analytical model, results are discussed, using preliminary data from commercially available motors. A wide range of possible motor designs using a detailed two-dimensional magneto static FE simulation.

The paper is outlined as follows. Section II reports some preliminary tests on e-bike motors. Both thermal and mechanical performances are defined. Section III describes the analytical model of the Interior PM (IPM) motor, the geometry considered in this work. The design strategy and the analytic performance evaluation are included. Analytical results are compared to FE simulation for a test geometry in Section IV, then the full capabilities mapping is presented in Section V. The characteristics of the motor under test are included in the analysis and an improved design solution is presented. It yields a performance improvement, maintaining the same rare-earth material volume.

II. Preliminary Test on Commercial Motors

As defined by EU regulations, the electric assistance is limited to a maximum speed of 25 $\mathrm{km/h}$ and a maximum power of 250 W. Even though the continuous power of the motor is limited, the motor drive is designed to exhibit temporary power that is much higher. The battery is usually a low-voltage lithium-ion. Although 48 V-batteries are becoming popular, a typical DC bus voltage has 36 V.

Experimental tests are performed on a commercial motor with the 12 slots/14 poles configuration and an Interior Permanent Magnet (IPM) rotor geometry. Both thermal and electro-mechanical measures are carried out.

The test bench arrangement is reported in Fig. 1. The test setup consists of a torque sensor, a master motor, and a slave motor, each with its inverter, running on a three-phase power supply. The torque sensor measures applied torque. The master motor drives the system, while the slave motor aids in load simulation, controlled by their respective inverters for precise operation.

A. Thermal test

Fig. 2 shows thermal test on the stator winding, carried out to identify the rated current. The thermal test was performed with a locked-rotor motor. Temperature was sampled until reaching the steady-state value. The environmental temperature is 20 °C and the motor is thermally insulated as it can be compared to a closed system.

Fig. **??** shows the DC supply for the thermal measurement. The DC current supplied is selected to have a condition similar

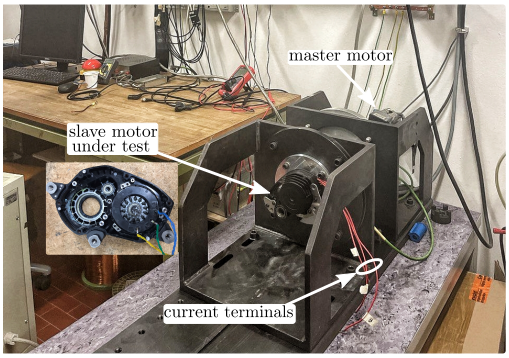

Fig. 1. Test bench for the commercial motor.

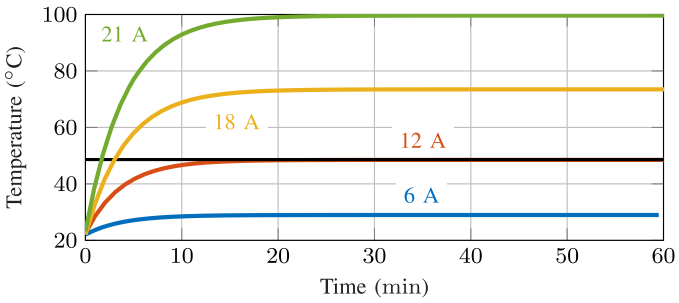

Fig. 2. Measured temperature versus time.

to the AC current supplied. The DC currents can be compared to the AC currents in the instant represented in Fig. **??**. Comparing phase currents of Fig. **??** and Fig. **??**:

$$\frac{2}{3}\cdot I_{DC} = \frac{\hat{I}_{AC}}{\sqrt{3}} \quad \Rightarrow \quad \hat{I}_{AC} = \frac{\sqrt{3}}{2}\cdot I_{DC} \tag{1}$$

Imposing a 12 A peak current the steady-state temperature rise reached (55 °C) can be sustained during nominal operation. Such current corresponds to a RMS current density of 7.5 $\mathrm{A/mm^2}$. Thus, this current value is considered to be the nominal current of the motor.

Fig. 2 also shows two additional measures feeding the winding with 6 A peak, 18 A peak and 21 A peak. The steady-state temperature rises are 30 °C, 75 °C and 100 °C, respectively. The 21 A peak can be sustained for a maximum time of 5 min, when the temperature rise reaches 100 °C.

B. Mechanical capabilities test

Trough the test bench of Fig. 1, the motor has been supplied by several d-axis and q-axis currents, $\mathrm{i_d}$ and $\mathrm{i_q}$. In Fig. 3a, such current coordinates are represented as dots in the $\mathrm{i_d}-\mathrm{i_q}$ plane. The torque is measured for each $\mathrm{i_d}-\mathrm{i_q}$ point, in Fig. 3a some torque levels are reported. Flux-linkages are measured as well, reported in Fig. 3b. From these two maps the torque and power versus speed capabilities are derived.

Torque (Fig. 3c) and power (Fig. 3d) are computed considering a DC bus voltage of 36 V. A voltage drop equal to 5 % is taken into account.

When the 12 A peak current is supplied the torque delivered is 1 N m, while with the current 18 A peak it is 1.5 N m and with 21 A peak it is 1.72 N m. The rated speed is about

TABLE I
IPM SPOKE MOTOR EXPERIMENTAL TEST RESULTS.

Current peak (A)	Current density rms (A/mm^2)	Torque (N m)	Power peak (W)	Temperature rise (°C)
12	7.5	1	360	55
18	11	1.49	550	75
21	13	1.72	650	100

TABLE II
MOTOR CONFIGURATION PARAMETERS AND GEOMETRY.

Parameter	Symbol	Value	Unit
Number of slots	Q_s	12	–
Number of poles	$2p$	14	–
External diameter	D_e	80	mm
Shaft diameter	D_{sh}	10	mm
Stack length	L_{stk}	20	mm
Air gap length	g	0.5	mm
PM thickness	t_m	3	mm
PM remaining flux	B_{rem}	1.12	T
PM relative permeability	μ_{rec}	1.06	-
Max value in tooth	B_t	1.8	T
Max value in back-iron	B_{bi}	1.6	T
base speed	n	3000	rpm

3000 rpm. The output power is 360 W when the 12 A peak current is supplied, 550 W when the 18 A peak current is supplied and 650 W when the 21 A peak current is supplied, reaching magnetic saturation.

TABLE I summarizes all measures, including electrical inputs and mechanical and thermal outcomes from the motor. In addition, in the figures described, dashed lines represent finite element simulation results. The motor model employed for such simulations is presented in Section V.

III. ANALYTICAL MODEL OF THE IPM MOTOR

A. Motor geometry specifications

The spoke-type IPM motor is studied. The main design parameters and material properties are summarized in TABLE II. The base speed considered is 3000 rpm, corresponding to a frequency of 250 Hz.

Since the PMs are arranged radially (a spoke disposition) they produce a tangential flux and the magnetizing flux produced by one PM is added to that produced by the adjacent PM, resulting in the so-called concentrated flux configuration. This geometry yields a high volume of PMs, and consequently a high torque density, which is highly desired in electric bicycle applications.

The following conditions are considered for the design analysis. First, the current density is fixed to a nominal value of 7.5 A/mm^2, that is a typical value to avoid high temperatures. Then, the PM thickness t_m is fixed 3 mm. Finally, the parameter space includes the PM height h_m and the inner stator diameter D.

B. Motor analytic model and design

The analytical model employed to compute the flux density, the torque, and power losses is described hereafter. A lumped-

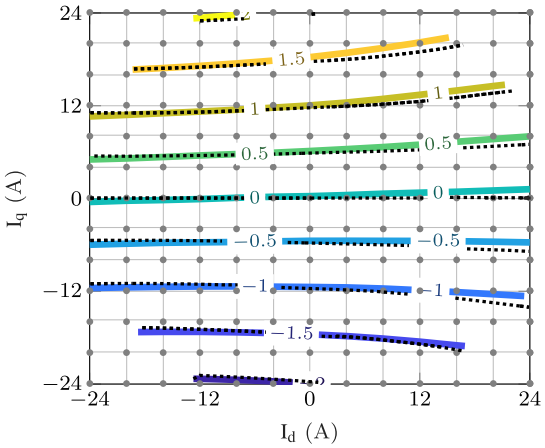

(a) Torque map measured.

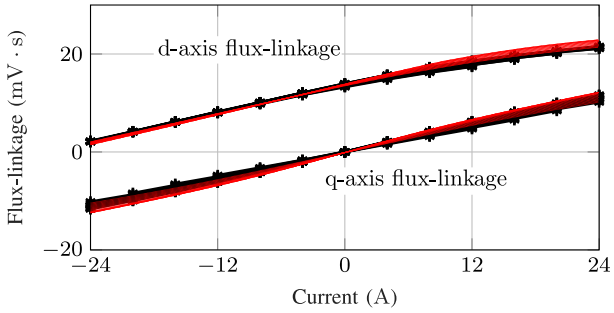

(b) Flux-linkages map measured.

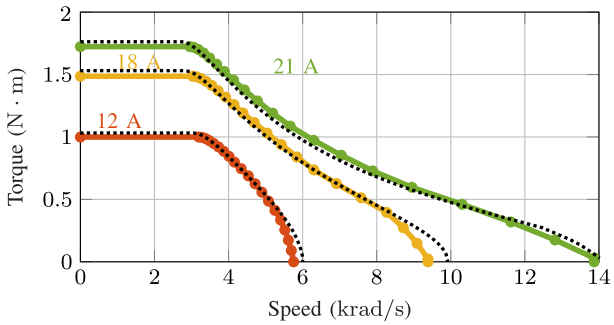

(c) Torque vs speed.

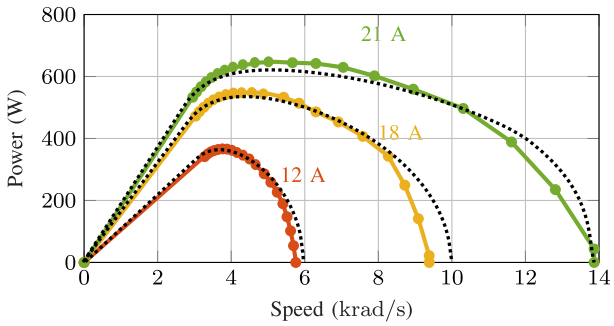

(d) Power vs speed.

Fig. 3. Experimental tests on a 12 slots/14 poles commercial motor (dots refer to the measured points and dashed lines refer to simulations).

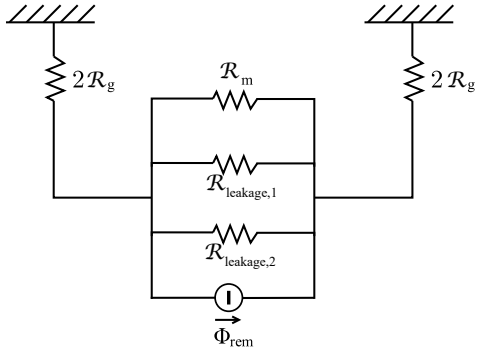

Fig. 4. IPM spoke motor MEC.

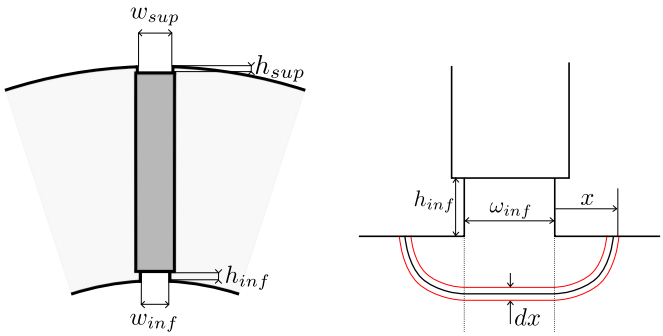

(a) IPM spoke detail.

(b) Leakage flux approximation for the MEC.

Fig. 5. IPM spoke motor model.

parameters Magnetic Equivalent Circuit (MEC) is defined, reported in Fig. 4.

The air gap is modelled as a reluctance $\mathcal{R}_g$. The PM is modelled as a reluctance $\mathcal{R}_m$ in parallel to a flux generator Φ_{rem} and to two reluctances which take into account the leakage flux. Two PMs are represented in parallel, as they both contribute to the flux per pole. As observed in Fig. 5a the geometry includes two air gaps above and below the PM, which cause leakage flux. Since the most of leakage flux passes through the inferior gap, the reluctance associated to the superior gap is neglected. $\mathcal{R}_{leakage,1}$ takes into account the leakage flux along the gap of h_{inf} thickness, while $\mathcal{R}_{leakage,2}$ takes into account the leakage flux lines enclosed by the red line represented in Fig. 5b.

The reluctance associated to the leakage flux along the thickness w_{inf} is computed as:

$$\mathcal{R}_{leakage,1} = \frac{w_{inf}}{\mu_0 \cdot h_{inf} \cdot L_{stk}} \tag{2}$$

The second leakage reluctance is obtained differently. The permeance along the leakage flux line can be computed as the integral of the infinitesimal permeances along the volume of the tube of Fig. 5b. Along half pole pitch $p_s/2 = \pi D/(2Q)$ there are two sections, two equal to a quarter of circumference and one equal to a straight line. The permeance is computed through the integral along these sections:

$$\begin{aligned}\mathcal{P}_{leakage,2} &= \int_0^{p_s/2} d\mathcal{P} = \int_0^{p_s/2} \mu_0 \cdot \frac{dx \cdot L_{stk}}{\pi \cdot x + w_{inf}} \\ &= \frac{\mu_0 \cdot L_{stk}}{\pi} \cdot \ln\left(\frac{\pi^2 D}{2Q w_{inf}} + 1\right)\end{aligned} \tag{3}$$

Then, the reluctance associated to the leakage flux is $\mathcal{R}_{leakage,2} = 1/\mathcal{P}_{leakage,2}$.

The equivalent reluctance which takes into account the leakage flux $\mathcal{R}_{leakage}$ is computed as the parallel between $\mathcal{R}_{leakage,1}$ and $\mathcal{R}_{leakage,2}$. The air gap flux Φ_g results from the sum of the flux generated by both spoke-type PMs, as such IPM rotor configuration is also called concentrated flux machine. Fig. 4 shows the final MEC model developed. Its solution is:

$$\Phi_g = \Phi_{rem} \cdot \frac{\mathcal{R}'_m}{2 \cdot \mathcal{R}_g + \mathcal{R}'_m} \tag{4}$$

where the reluctance $\mathcal{R}'_m$ results from the parallel between $\mathcal{R}_m$, $\mathcal{R}_{leakage,1}$ and $\mathcal{R}_{leakage,2}$ (i. e. the parallel between $\mathcal{R}_m$ and $\mathcal{R}_{leakage}$). Finally, the air gap flux density is computed as $B_g = \Phi_g / S_g$.

After calculating the flux density of the air gap, all geometric parameters can also be computed as described in Section III B of [24]. They are obtained based on the flux-density limit along the teeth and the back-iron. Section III C of [24] describes the torque and efficiency computation, including copper and iron losses estimation.

IV. Analytical and FEA results

A. No-load flux density

First of all the air gap flux density computed analytically is compared to the one from FE simulations, considering a zero stator currents. The air gap flux density has a quasi-squared waveform, since it is equal to the peak only along the surface of the air gap in front of the magnet, while it drops between two opposite poles.

Fig. 6 shows the comparison of the flux density waveform computed analytically and by means of FE analysis for a test geometry. Its parameters are 12 slots, 14 poles, $h_m = 7$ mm and $D = 45$ mm. Two different FE simulations are carried out: one with iron linearity and without stator slots (called *FE linear*), another with non-linear material properties and with stator slots effect (called *FE non linear*). The non linear result is similar to the analytical result. The slot effect is visible only in non linear FE result.

The maximum constant value of the flux density waveform equals to 0.869 T for the analytic computation, 0.872 T for the linear FE simulation and 0.866 T for the non linear FE simulation. Comparing the first harmonic amplitude, the analytic results 1.05 T, from linear FE simulation is 1.08 T while from the non linear FE simulation it results 1.07 T.

B. Output torque and losses

Fig. 7 shows the comparison of the output torque versus the rotor position for the test motor configuration. The FE torque

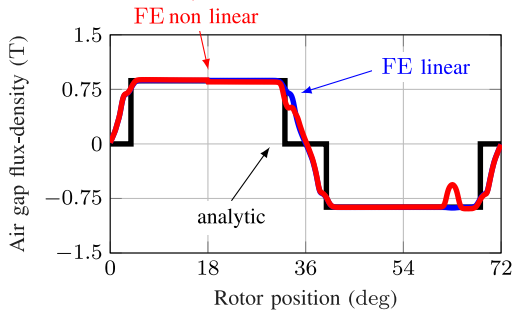

Fig. 6. Air gap flux density waveform, analytic and FE comparison.

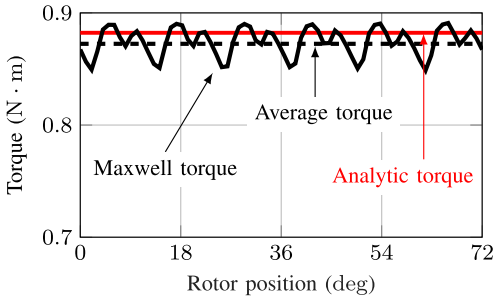

Fig. 7. Torque versus rotor position, analytic and FE comparison.

is computed by the Maxwell stress tensor, which includes the reluctance component. Its average value is very close to the analytical prediction, with only a 2 % difference.

Concerning copper losses, the analytical model esteems 16.3 W of losses, while FEA losses are 16 W. Analytical iron losses are equal to 9.9 W, while FE 8 W. As a result, the analytical efficiency corresponds to the FE results, being 86 % and 87 %, respectively.

V. Performance Mapping

The IPM motor performance is computed at a fixed current density 10 $\mathrm{A/mm^2}$, varying the PM height 7 mm − 20 mm and the stator internal diameter 35 mm to 65 mm. Feasibility is verified as

$$D/2 \geq D_{sh}/2 + g + (h_m + h_{sup} + h_{inf}) \tag{5}$$

The 12 poles and 14 poles machine is analysed hereafter.

A. Parameter space performance mapping

Fig. 8 shows the torque map with respect to the diameter ratio (stator inner diameter versus external diameter D/D_e) and the PM length. Blank areas represent the diameter and PM length combinations leading to non feasible geometries. The analytical torque has a good match with the FE torque. The PM length and the diameter ratio of the tested motor are identified in the map. Their values are 9 mm and 0.59. Observing the map, some alternative design solutions are recognizable.

Alternative design 1. Maintaining the PM length of the tested motor, but reducing the diameter ratio. The PM length is equal to 9 mm. Decreasing the diameter ratio from 0.59 to 0.5,

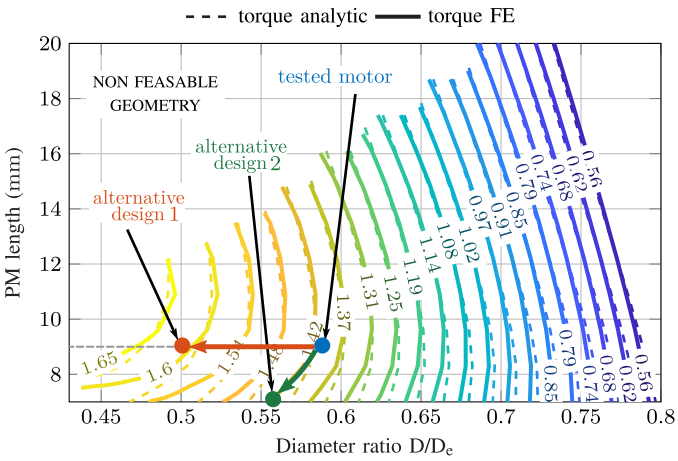

Fig. 8. Comparison of analytic (dashed lines) and FE (solid lines) torque map, varying the diameter ratio and the PM length.

the torque increases of 15 %, from 1.42 N · m to 1.6 N · m, without any change in the overall magnetic volume.

Alternative design 2. Moving along the iso-torque curve. Fixing a desired value for the torque, the PM length (thus the magnetic material volume) can be minimized selecting the optimal diameter ratio. The iso-torque curve level is 1.42 N · m. The magnet volume can be reduced selecting a lower diameter ratio: 7 mm are sufficient with a diameter ratio 0.55, delivering the same torque.

Fig. 9 shows both copper and iron losses, mapped in the parameter space. They are computed through a combination of analytic model and simulation. Copper losses are computed analytically, since two-dimensional simulations do not include the end-winding impact on overall Joule losses. Iron losses are computed through Steinmetz law, which takes into account the saturation effect. Indeed, they depend on the flux density in the back-iron and teeth, which are extracted from the output of finite element simulation.

Joule losses (Fig. 9a) decrease as the diameter ratio increases. In fact, the copper volume is lower when stator slots become smaller, since the current density is fixed. At the same time, fixing the diameter, Joule losses decrease as PM length increases, since the slot cross-section area slightly decreases. In fact, fixing the diameter value, the air gap flux density increases as the PM length increases. Consequently, the tooth width and the back-iron height have to increase to avoid saturation of the stator core. This leads to a slight decrease of the slot area, to compensate the higher magnetizing flux. A lower slot area yields a lower copper volume, thus lower Joule losses.

Iron losses (Fig. 9b) depend only on the flux-density, since simulations are carried out at a fixed frequency. Once the PM length is fixed, iron losses do not change with the diameter ratio, as the flux-density in teeth and back-iron is kept constant by designing these two properly. Differently, when the PM length increases, iron losses increase as saturation phenomena occur. Therefore, the dependence of iron losses on inner diameter and PM length is opposite to the variation of Joule losses. Consequently, the overall efficiency will mainly depend

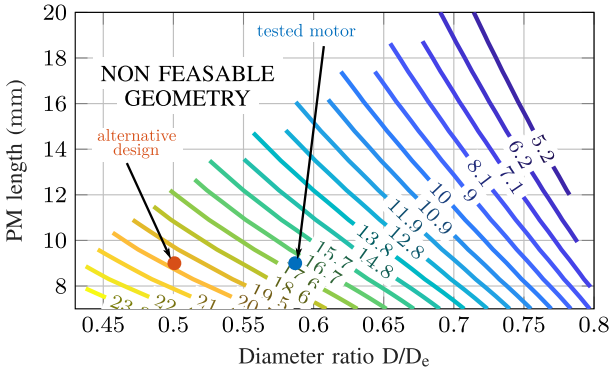

(a) Copper losses.

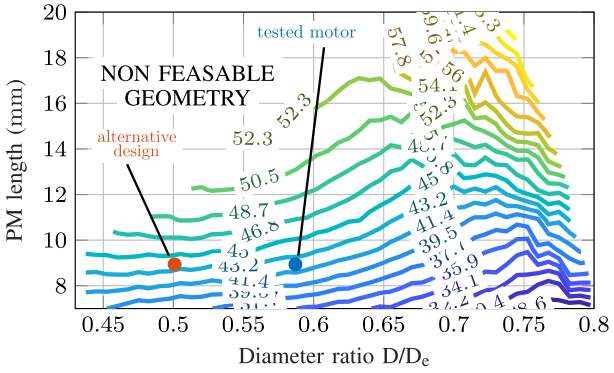

(b) Iron losses.

Fig. 9. Losses mapping in the parameter space, FE results.

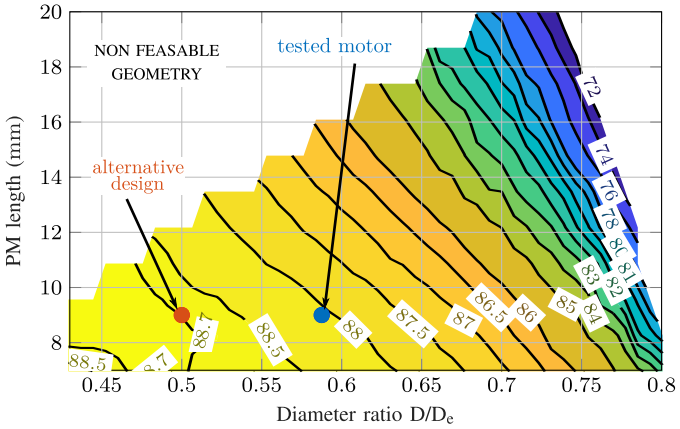

Fig. 10. FE efficiency map varying the diameter ratio and the PM length.

on the power delivered.

Fig. 10 shows the efficiency map computed from FE analysis results. It is worth noticing that the efficiency map is similar to the torque map. In the parameter space considered, the designed motors are characterized by a minimum efficiency of 70 % and a maximum efficiency of 88.7 %. Moving to higher torque regions, the efficiency exhibits a slight improvement as well. However, comparing the tested motor parameters with the alternative design parameters, the efficiency increase is lower than 1 %.

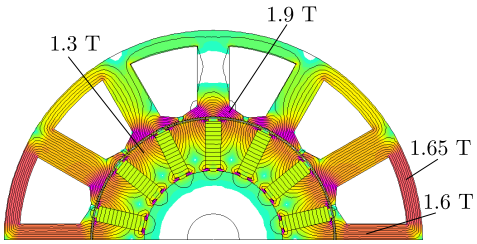

(a) Tested motor.

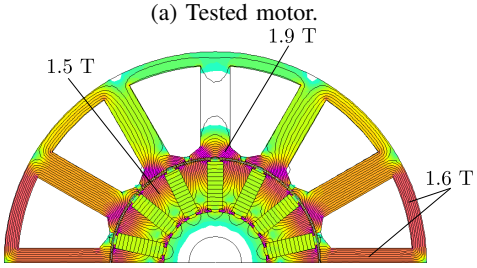

(b) Alternative design.

Fig. 11. Comparison of iron flux density.

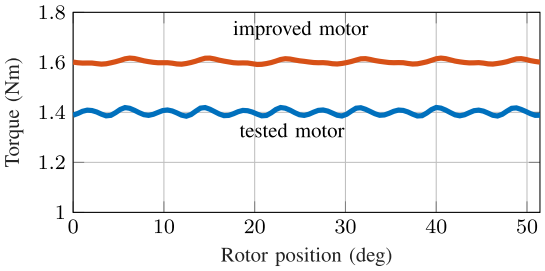

(a) Torque versus rotor position.

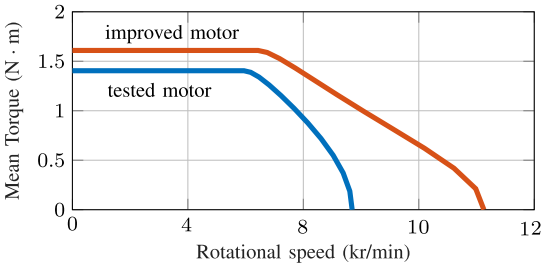

(b) Torque versus speed characteristic.

Fig. 12. Torque characteristics comparison between two geometries.

B. Comparison of two solutions

The two design solutions presented above are compared in greater detail. It is worth noticing that the simulated machine has a simple design, while the tested motor has a more complex, well-shaped, and optimized structure. Fig. 11 shows the two motors geometry. PMs have the same dimensions, 3 mm × 9 mm. The inner stator diameter is equal to 47 mm for the tested motor, and 40 mm for the improved design. Consequently, stator slot areas are different: the alternative machine has a higher slot area and lower tooth width and back-iron length. Flux-density values are similar in the stator iron sheet, since the design is tuned in order to maintain almost the same flux-density in teeth and back-iron. Differently, rotor iron flux-density is higher for the machine with the lower diameter ratio, as expected.

Fig. 12a shows the torque varying the rotor position. Av-

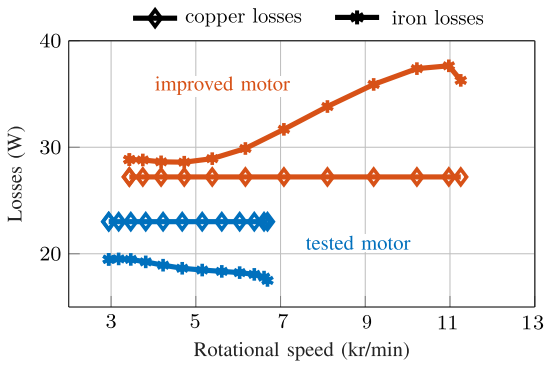

Fig. 13. Copper and iron losses versus speed during flux-weakening operation, comparison between the two geometries.

erage torque is $1.4\ \mathrm{N \cdot m}$ for the tested motor and $1.6\ \mathrm{N \cdot m}$ for the improved geometry, leading to an increase of $15\ \%$, as already discussed. Even if the motor configuration is the same and the rotor geometry is equal, the torque ripple is lower for the improved machine. The peak to peak torque decreases from $0.035\ \mathrm{N \cdot m}$ to $0.025\ \mathrm{N \cdot m}$, while compared to the average torque the percentage ripple $2.5\ \%$ is reduced to $1.6\ \%$.

Both motors can achieve flux-weakening operation. The nominal current angle is increased until the maximum speed is reached, at zero torque level. The improved geometry is characterized by higher speed and torque characteristic, as observed in Fig. 12b. From the base speed of about $3000\ \mathrm{rpm}$, such a motor can run up to $7000\ \mathrm{rpm}$. The other machine reaches the maximum speed $4800\ \mathrm{rpm}$ with a zero torque delivered, while the improved motor can still deliver about $1\ \mathrm{N \cdot m}$.

Fig. 13 shows losses during flux-weakening operation. Since the alternative motor design has an improved flux-weakening, its losses cover a more extended range of speeds. Joule losses are constant since the current supplied changes only the angle but no the amplitude. The improved machine Joule losses amount to $27\ \mathrm{W}$, while for the other motor they are lower, equal to $23\ \mathrm{W}$.

Iron losses of the improved motor increase with the speed. Differently, they slightly decrease for the tested motor because the flux-density decreases more than the speed increases.

VI. Conclusion

This paper describes a design procedure of electric motors for e-bike applications, focusing on permanent magnet synchronous motors. The proposed procedure combines an analytical model of the motor with finite element simulations to properly predict the motor performance. Experimental measurements are presented to validate the model of the motor. Then, various motor geometries are analysed. The main objective of this paper is to provide a design guideline and to identify a design region to achieve a performance improvement of e-bike motors. Based on the proposed procedure it is possible to determine the more convenient geometry of the motor, according to fixed constrains. As an example, the capabilities of a motor have been tested and compared to those estimated modifying its geometry, to the aim of increase the average torque, and remaining within geometrical constrains.

References

[1] W. C. Morchin and H. Oman, *Electric bicycles: a guide to design and use*. Electric Bicycle Manual, 2006, vol. 8.

[2] (2021) Projections for the global electric bike market between 2018 and 2028. [Online]. Available: https://www.statista.com/statistics/1261084/global-e-bike-market-forecast/

[3] A. Vagati, G. Franceschini, I. Marongiu, and G. P. Troglia, "Design criteria of high performance synchronous reluctance motors," in *Conf. Rec. IEEE-IAS Annu. Meeting*, vol. 1, 1992, pp. 66–73.

[4] A. Muetze and Y. C. Tan, "Electric bicycles - a performance evaluation," *IEEE Industry Applications Magazine*, vol. 13, no. 4, pp. 12–21, 2007.

[5] ——, "Modeling and analysis of the technical performance of DC-motor electric bicycle drives based on bicycle road test data," in *2007 IEEE International Electric Machines Drives Conference (IEMDC)*, vol. 2, 2007, pp. 1574–1581.

[6] E. Starschich and A. Muetze, "Comparison of the performances of different geared brushless-DC motor drives for electric bicycles," in *2007 IEEE International Electric Machines Drives Conference (IEMDC)*, vol. 1, 2007, pp. 140–147.

[7] K. F. I. Faruque, N. Nawshin, M. F. Bhuiyan, M. R. Uddin, M. Hasan, and K. M. Salim, "Design and development of bldc controller and its implementation on e-bike," in *2018 International Conference on Recent Innovations in Electrical, Electronics and Communication Engineering (ICRIEECE)*, 2018, pp. 1461–1465.

[8] S. K. Chawrasia, A. Das, and C. Kumar Chanda, "Design and analysis of electric bike hub-motor using motor-cad," in *2020 3rd International Conference on Energy, Power and Environment: Towards Clean Energy Technologies*, 2021, pp. 1–6.

[9] R. Nasiri-Zarandi, A. Karami-Shahnani, M. S. Toulabi, and A. Tessarolo, "Design and experimental performance assessment of an outer rotor pm-assisted synrm for the electric bike propulsion," *IEEE Transactions on Transportation Electrification*, vol. 9, no. 1, pp. 727–736, 2023.

[10] A. M. EL-Refaie, "Fractional-slot concentrated-windings synchronous permanent magnet machines: Opportunities and challenges," *IEEE Transactions on Industrial Electronics*, vol. 57, no. 1, pp. 107–121, 2010.

[11] S.-o. Kwon, S.-i. Kim, P. Zhang, and J.-p. Hong, "Performance comparison of ipmsm with distributed and concentrated windings," in *Conference Record of the 2006 IEEE Industry Applications Conference Forty-First IAS Annual Meeting*, vol. 4, 2006, pp. 1984–1988.

[12] A. Di Gerlando, R. Perini, and M. Ubaldini, "High pole number, pm synchronous motor with concentrated coil armature windings," in *Recent Developments of Electrical Drives*. Springer, 2006, pp. 307–320.

[13] S. Koyuncu, U. Tuncer, A. Dalcali, and S. Oncu, "External rotor 6/8 switched reluctance motor design for e-bike," in *2021 10th International Conference on Renewable Energy Research and Application (ICRERA)*, 2021, pp. 131–135.

[14] B. Howey, B. Bilgin, and A. Emadi, "Design of an external-rotor direct drive e-bike switched reluctance motor," *IEEE Transactions on Vehicular Technology*, vol. 69, no. 3, pp. 2552–2562, 2020.

[15] D. Michieletto and L. Alberti, "Design and realization of a synchronous reluctance motor with printed rotor," in *IECON 2022 – 48th Annual Conference of the IEEE Industrial Electronics Society*, 2022, pp. 1–7.

[16] ——, "On the performance of PMAREL and REL synchronous motor prototypes with printed rotor," in *2023 IEEE Energy Conversion Congress and Exposition (ECCE)*, 2023, pp. 3953–3958.

[17] S. B. Bhat, S. P. Nikam, and B. G. Fernandes, "Design and analysis of ferrite based permanent magnet motor for electric assist bicycle," in *2014 International Conference on Electrical Machines (ICEM)*, 2014, pp. 106–111.

[18] R. Wilson, R. Gandhi, A. Kumar, and R. Roy, "Design and analysis of twin-rotor axial flux permanent magnet synchronous motor for electric bicycle using 3d finite element analysis," in *2020 IEEE International Conference on Power Electronics, Smart Grid and Renewable Energy (PESGRE2020)*, 2020, pp. 1–6.

[19] N. K. Tung, J.-Y. Lee, J.-H. Lee, and Y.-D. Chun, "Design of a 300w axial flux motor for an electric bike," in *2021 24th International Conference on Electrical Machines and Systems (ICEMS)*, 2021, pp. 23–28.

[20] S. H. Rhyu, S. Khaliq, R. E. Kim, and K. D. Lee, "Design and analysis of axial flux permanent magnet motor for electric bicycles with hybrid stator core," in *2017 20th International Conference on Electrical Machines and Systems (ICEMS)*, 2017, pp. 1–6.

[21] R. Nasiri-Zarandi, A. Karami-Shahnani, M. S. Toulabi, and A. Tessarolo, "Design and experimental performance assessment of an outer rotor pm-assisted synrm for the electric bike propulsion," *IEEE Transactions on Transportation Electrification*, vol. 9, no. 1, pp. 727–736, 2023.

[22] Y. Yang, M. M. Rahman, T. Lambert, B. Bilgin, and A. Emadi, "Development of an external rotor v-shape permanent magnet machine for e-bike application," *IEEE Transactions on Energy Conversion*, vol. 33, no. 4, pp. 1650–1658, 2018.

[23] (2022) Bosch ebike systems. [Online]. Available: https://www.bosch-ebike.com/it/

[24] C. Contò and N. Bianchi, "Design of electric motor for e-bike application," in *2023 IEEE International Electric Machines and Drives Conference (IEMDC)*, 2023, pp. 1–7.

[25] ——, "Overload capability test of a permanent magnet synchronous motor for e-bike application," in *2023 IEEE International Electric Machines and Drives Conference (IEMDC)*, 2023, pp. 1–7.